AN UPPER BOUND APPROACH FOR ANALYSIS OF HYDROFORMING OF SHEET METALS

A. Assempour, M. Bagherzadeh and M.R. Emami

Center of Excellence in Design, Robotics and Automation, Department of Mechanical Engineering
Sharif University of Technology, Tehran, Iran, assem@sharif.edu

(Received: January 9, 2004 – Accepted in Revised Form: October 14, 2004)

Abstract Considering a kinematical velocity admissible field, the upper bound method has been used for predicting the amount of pressure in hydroforming of sheet metals. The effects of work hardening, friction and blank size have been considered in pressure prediction. Also the effect of sheet thickness variation has been considered in the present work formulations. The relation between pressure and punch stroke has been obtained and optimized by changing the selective parameters in the velocity components. The results for cylindrical and hemispheric parts have been obtained and compared with the published experimental results. The effects of work hardening, friction and blank size on hydroforming pressure have been examined on an elliptical part. Good agreement was found between the experimental and numerical results.

Key Words Hydroforming, Sheet Metals, Upper Bound, 3D Strain, Work Hardening, Thickness Variation

چکیده در فرایند هیدروفرمینگ ورقهای فلزی با در نظر گرفتن یک میدان سرعت سازگار، از روش کران بالا برای تخمین فشار مورد نیاز استفاده شده است. اثر پارامترهای مختلف نظیر نمای کار سختی، قطر بلانک اولیه و ضریب اصطکاک در محاسبات فشار در نظر گرفته شده اند. همچنین اثر تغییر ضخامت در حین فرمدهی در محاسبات کرنش در نظر گرفته شده است. رابطه بین فشار شکل دهی و جابجایی پانچ با توجه به کمینه سازی انرژی مصرفی توسط پارامترهای انتخابی در مولفه های سرعت بدست آمده است. در محاسبات فشار در قطعات استوانه ای و نیم کره ای نتایج حاصل شده با نتایج تجربی موجود در مراجع مقایسه گردیده است. هر دو نتایج تجربی و عددی مطابقت خوبی را نشان می دهند. اثر پارامترهای کار سختی، قطر بلانک اولیه و ضریب اصطکاک در محاسبات فشار در یک قطعه بیضوی مورد بررسی قرار گرفته شدند .

1. INTRODUCTION

Nowadays hydroforming is an efficient process in metal forming. As regards uniform thickness distribution in this process, it uses specially in forming of airplane parts. J.Tirosh et al. [1] found an appropriate relationship for punch stroke vs. fluid pressure in order to obtain uniform sheet thickness in axisymmetric hydroforming. They also studied the effects of workhardening exponent, friction coefficient and blank size.

For hydroforming of general noncircular cups there has been no analytic and systematic method to study pressure vs. punch stroke curve.

Recently, analyses have been proposed for hydroforming of prismatic and longitudinally curved boxes with regular polygonal cross-section based on the assumption of uniform thickness [2, 3].

T.S.Noh et al. [4] also found an appropriate relationship for punch stroke vs. fluid pressure in order to obtain uniform sheet thickness in parts with general shapes.

In the present work, an investigation has been made on predicting of hydroforming pressure in general shaped parts with analytic punch surface. The bases of formulation are similar to formulations used by T.S.Noh et al. [4]. They assumed the sheet thickness does not vary during the hydroforming process. However, in this work, this variation has been considered in the formulation. Therefore, in the present work the strain components are considered three dimensionally. The results for cylindrical and hemi-spherical parts have been obtained and compared with the published experimental

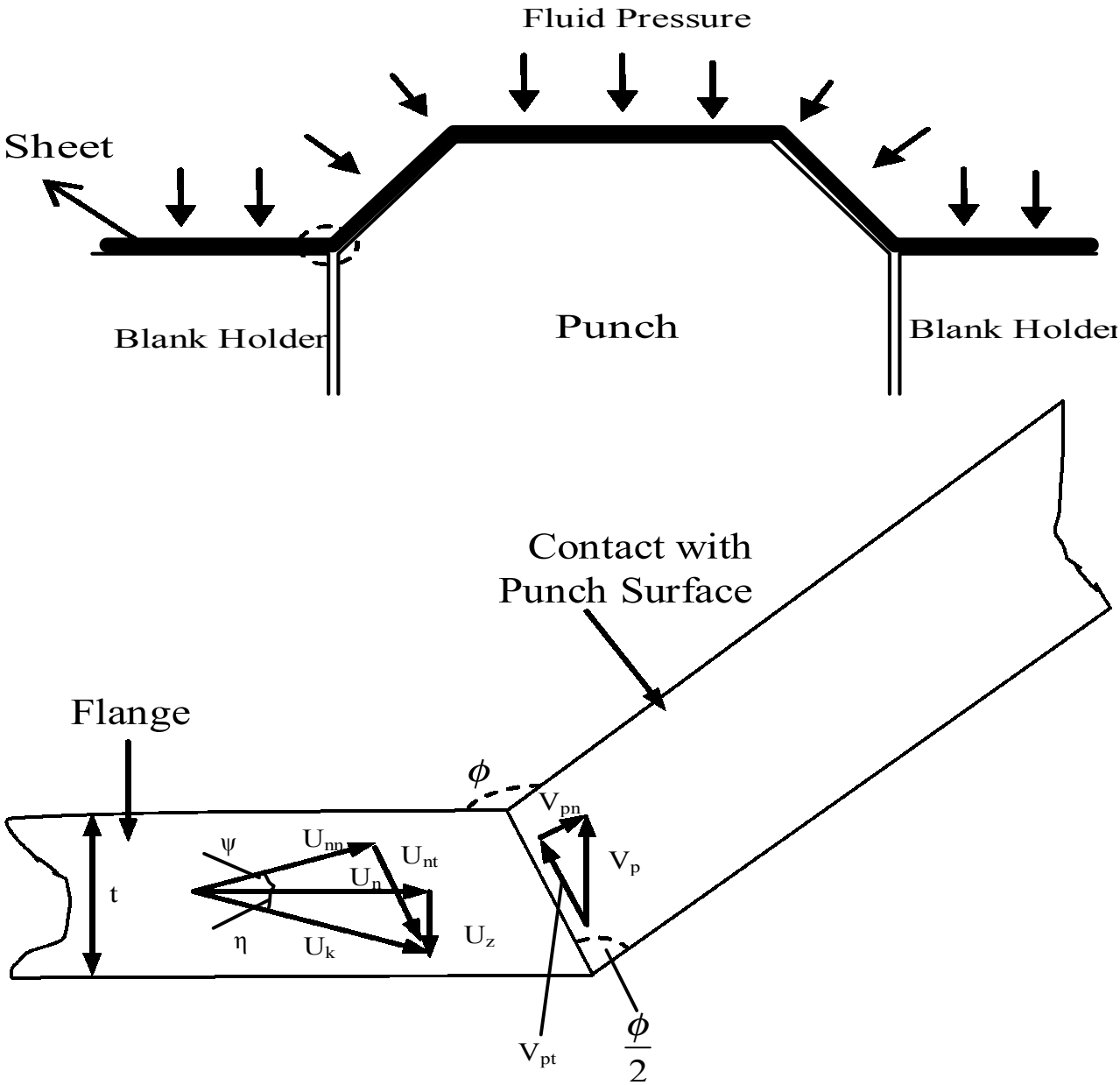

Figure 1. Surface of velocity discontinuity.

results. Analysis has also been performed on an elliptic part and the results have qualitatively been investigated.

2. BASIC GEOMETRICAL AND KINEMATICAL FORMULATION

In order to analyze hydroforming, some simplifying assumptions are considered. a) The sheet material in contact with the punch is assumed to be rigid, i.e., to undergo no plastic deformation. In fact, due to very high fluid pressure, it can be assumed that material sticks to the punch and no plastic flow takes place. b) At any stage of punch movement, in analysis, the flat sheet that located on blank holder intersects the punch as a sharp edge which is called the boundary of velocity discontinuity (see Figures 1 and 2).

Assume that the punch surface or sheet surface is

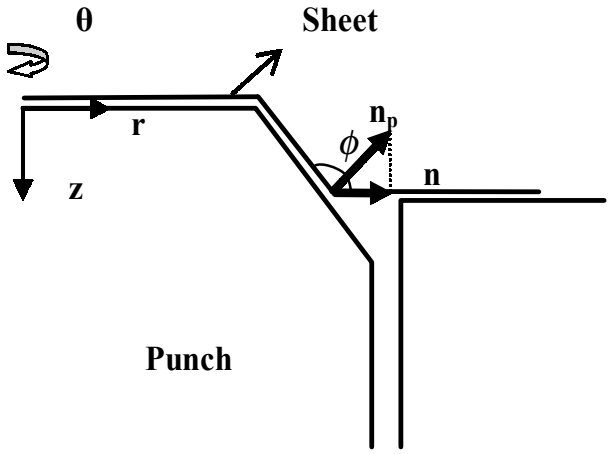

Figure 2. Hydroforming Geometry.

expressed generally in the cylindrical coordinates in the following analytical form:

$$F(r,\theta,z)=0 \tag{1}$$

The unit normal vector at the punch surface is given by:

$$\vec{n}_p=\frac{\overrightarrow{\nabla F}}{|\overrightarrow{\nabla F}|}=\frac{\frac{\partial F}{\partial r}\vec{e}_r+\frac{1}{r}\frac{\partial F}{\partial \theta}\vec{e}_\theta+\frac{\partial F}{\partial z}\vec{e}_z}{\sqrt{(\frac{\partial F}{\partial r})^2+(\frac{1}{r}\frac{\partial F}{\partial \theta})^2+(\frac{\partial F}{\partial z})^2}} \tag{2}$$

A normal vector, **n**, which is projection of $\mathbf{n_p}$ on the flange surface at z=h defines as follow:

$$\vec{n}=\frac{\frac{\partial F}{\partial r}\vec{e}_r+\frac{1}{r}\frac{\partial F}{\partial \theta}\vec{e}_\theta}{\sqrt{(\frac{\partial F}{\partial r})^2+(\frac{1}{r}\frac{\partial F}{\partial \theta})^2}} \tag{3}$$

n, is perpendicular to the edge of velocity discontinuity and located on the flange surface:

Figure 2 shows the geometrical relationship between $\mathbf{n_p}$ and **n**. let us ϕ be an angle between the punch surface (as represented by an intersection curve between the punch surface and the plane composed of two normal vectors $\mathbf{n_p}$ and **n**) and the plane of the flange at z=h. Then the angle ϕ is related with $\mathbf{n_p}$ and **n** as follows:

$$\mathrm{Sin}\phi=\mathrm{Cos}(\phi-\frac{\pi}{2})=\vec{n}_p.\vec{n}=\frac{\sqrt{(\frac{\partial F}{\partial r})^2+(\frac{1}{r}\frac{\partial F}{\partial \theta})^2}}{\sqrt{(\frac{\partial F}{\partial r})^2+(\frac{1}{r}\frac{\partial F}{\partial \theta})^2+(\frac{\partial F}{\partial z})^2}} \tag{4}$$

With use of trigonometric relations, the slope of the surface of velocity discontinuity at the angular position θ against the plane of flange z=h is determined as follows. (See Appendix A):

$$\tan(\frac{\phi}{2})=\sqrt{\frac{1-\mathrm{Cos}(\phi)}{1+\mathrm{Cos}(\phi)}}=\frac{\mathrm{Sin}\phi}{1+\mathrm{Cos}\phi}=\frac{\sqrt{(\frac{\partial F}{\partial r})^2+(\frac{1}{r}\frac{\partial F}{\partial \theta})^2}}{\sqrt{(\frac{\partial F}{\partial r})^2+(\frac{1}{r}\frac{\partial F}{\partial \theta})^2+(\frac{\partial F}{\partial z})^2}-\frac{\partial F}{\partial z}} \tag{5}$$

In order to consider effects of thickness variation, the inclination angle of velocity field to punch surface (see figure 1) is determined as follows:

$$\mathrm{Sin}(\eta)=\frac{u_z}{u_k} \tag{6}$$

u_z is a component of velocity that is in direction of thickness decrement and increases with increasing of inclination angle (the condition of u_z=0 is studied in ref. 4). The kinematical compatibility condition in surface of velocity discontinuity requires the equality of normal velocity components on both sides of surface of velocity discontinuity. This condition leads to the following relation (See Appendix B):

$$u_k=\frac{-V_p}{\tan(\frac{\phi}{2})\mathrm{Cos}\eta-\mathrm{Sin}\eta} \tag{7}$$

On the other hand u_k can again be expressed by considering the velocity components in the plane

which is normal to flange surface and also perpendicular to the edge of velocity discontinuity (Consider Equation 2):

$$u_k = \frac{\frac{\partial F}{\partial r}u_r + \frac{1}{r}\frac{\partial F}{\partial \theta}u_\theta + \frac{\partial F}{\partial z}u_z}{\sqrt{(\frac{\partial F}{\partial r})^2 + (\frac{1}{r}\frac{\partial F}{\partial \theta})^2 + (\frac{\partial F}{\partial z})^2}} \quad (8)$$

Then the velocity boundary conditions at the internal boundary of velocity discontinuity are given as (See Appendix C):

$$\frac{\partial F}{\partial r}u_r + \frac{1}{r}\frac{\partial F}{\partial \theta}u_\theta + \frac{\partial F}{\partial z}u_z = -\frac{\sqrt{(\frac{\partial F}{\partial r})^2 + (\frac{1}{r}\frac{\partial F}{\partial \theta})^2 + (\frac{\partial F}{\partial z})^2}}{\tan(\frac{\phi}{2})}. \quad (9)$$
$$(\sqrt{(u_z - V_p)^2 + u_z^2 \tan^2(\frac{\phi}{2})})$$

At: $F(r,\theta,z) = 0$

The incompressibility condition is given generally by the following equation:

$$\frac{\partial u_r}{\partial r} + \frac{1}{r}u_r + \frac{1}{r}\frac{\partial u_\theta}{\partial \theta} + \frac{\partial u_z}{\partial z} = 0 \quad (10)$$

The general form of solution for Equation 9 is given as (See Appendix D):

$$u_r = \frac{C}{r} + \sum_{i=1}^{\infty}\frac{a_i(r)}{r}\mathrm{Cos}(i\theta) + \sum_{i=1}^{\infty}\frac{b_i(r)}{r}\mathrm{Sin}(i\theta)$$
$$u_\theta = \sum_{i=1}^{\infty}\frac{db_i(r)}{dr}\frac{\mathrm{Sin}(i\theta)}{i} + \sum_{i=1}^{\infty}\frac{da_i(r)}{dr}\frac{\mathrm{Cos}(i\theta)}{i}$$
$$u_Z = -\sum_{i=1}^{\infty} z(\frac{da_i(r)}{rdr} + \frac{db_i(r)}{rdr})\mathrm{Cos}(i\theta) +$$
$$\sum_{i=1}^{\infty} z(\frac{da_i(r)}{rdr} - \frac{db_i(r)}{rdr})\mathrm{Sin}(i\theta) + a_0(\theta)b_0(r) \quad (11)$$

With consideration of the velocity boundary conditions of Equation 9, C, can be determined. Here, linear terms are taken for $a_i(r)$ and $b_i(r)$. Then the velocity components of Equation 11 are rewritten as:

$$u_r = \frac{C}{r} + \sum_{i=1}^{\infty}a_i\mathrm{Cos}(i\theta) + \sum_{i=1}^{\infty}b_i\mathrm{Sin}(i\theta)$$
$$u_\theta = \sum_{i=1}^{\infty}b_i\frac{\mathrm{Sin}(i\theta)}{i} + \sum_{i=1}^{\infty}a_i\frac{\mathrm{Cos}(i\theta)}{i}$$
$$u_Z = -\sum_{i=1}^{\infty} z(\frac{a_i + b_i}{r})\mathrm{Cos}(i\theta) +$$
$$\sum_{i=1}^{\infty} z(\frac{a_i - b_i}{r})\mathrm{Sin}(i\theta) + a_0 b_0 r\theta \quad (12)$$

Now, this velocity field can be applied to hydroforming of three-dimensional parts with arbitrary shapes, if surface of the punch is described in the analytic form. When the reference axis (θ=0) of the punch shape has an axis of symmetry, the odd function should vanish due to symmetric properties. The choice of terms should be considered in the velocity field where there are multiple axes of symmetry. Equations 12 satisfy the incompressibility and all the velocity boundary conditions. Therefore, Equations.12 are kinematically admissible. The strain rate components can also be given from derived velocity field:

$$\dot{\varepsilon}_r^* = \frac{du_r}{dr}$$
$$\dot{\varepsilon}_\theta^* = \frac{u_r}{r} \quad (13)$$
$$\dot{\varepsilon}_t^* = \frac{du_z}{d(\mathrm{thickness})}$$

3. UPPER BOUND

Using the upper bound theorem [6], the required forming pressure is:

$$P(h) = [\int_V \sigma_{ij}^* \dot{\varepsilon}_{ij}^* dv + \int_{s_r} k\Delta u^* ds_r] / [(A_n - A_p).V_p - \mu\int_{sf} u^* ds_f] \quad (14)$$

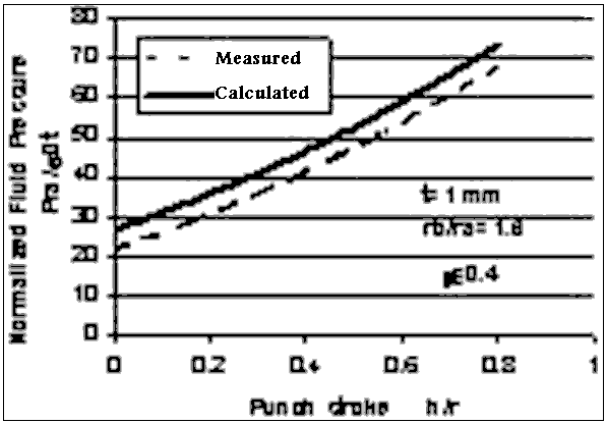

Figure 3. Measured [1] and calculated result for cylindrical part.

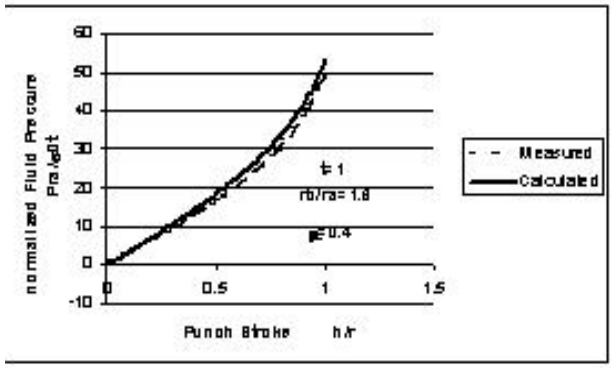

Figure 4. Measured [1] and calculated result for hemispheric part.

where, $\int_V \sigma_{ij}^* \dot{\varepsilon}_{ij}^* dv$ is the strain energy dissipation outside the punch, the second integral is the shear deformation energy due to velocity discontinuity and $\mu \int_{S_f} u^* ds_f$ is the waste of frictional energy under the blank holder surface. The surfaces subjected to blank holder pressure and fluid pressures are displayed in Figure 1. The surface of discontinuity can also be observed in the same Figure 1. The parameters, a_i and b_i, are subjected to optimization velocity so as to minimize the total power consumption. Velocity discontinuity component is obtained as follows (See Appendix E):

$$\Delta u^* = \sqrt{u_r^2 + u_\theta^2 + u_z^2 + u_k^2 \left(\frac{\cos^2\eta - \cos^2(\frac{\phi}{2})}{\cos^2(\frac{\phi}{2})}\right)} \quad (15)$$

Also surface element at the surface of velocity discontinuity is obtained as follows [4]:

$$ds_r = \frac{\sqrt{2}tr\sqrt{B - \frac{\partial F}{\partial z}\sqrt{B}}}{\sqrt{(\frac{\partial F}{\partial r})^2 + (\frac{1}{r}\frac{\partial F}{\partial \theta})^2}} d\theta \quad (16)$$

where:

$$B = (\frac{\partial F}{\partial r})^2 + (\frac{1}{r}\frac{\partial F}{\partial \theta})^2 + (\frac{\partial F}{\partial z})^2 \quad (17)$$

In solving of Equations four-point Gauss-Legendre integration [5] method has been used. Also in minimization of total power Nelder-Mead [5] method has been used. Appendix F displays the logic diagram of computations.

4. RESULTS

To evaluate the accuracy of the formulations, three types of shapes; consist of hemispheric, cylindrical and elliptic-circular boxes were studied. Table 1 reveals the information about the hemispheric and cylindrical parts [1]. The numerical and experimental results related to cylindrical part are given in Figure 3. In the figure, the pressure is normalized

TABLE 1. Conditions of Hemispheric and Cylindrical Parts [1].

Stress-Strain relation (kg/cm^2)	Friction Coefficient	Drawing ratio	Initial Blank radius (mm)	Initial Thickness (mm)
$3200\varepsilon^{0.15}$	0.4	1.65	124	1.00

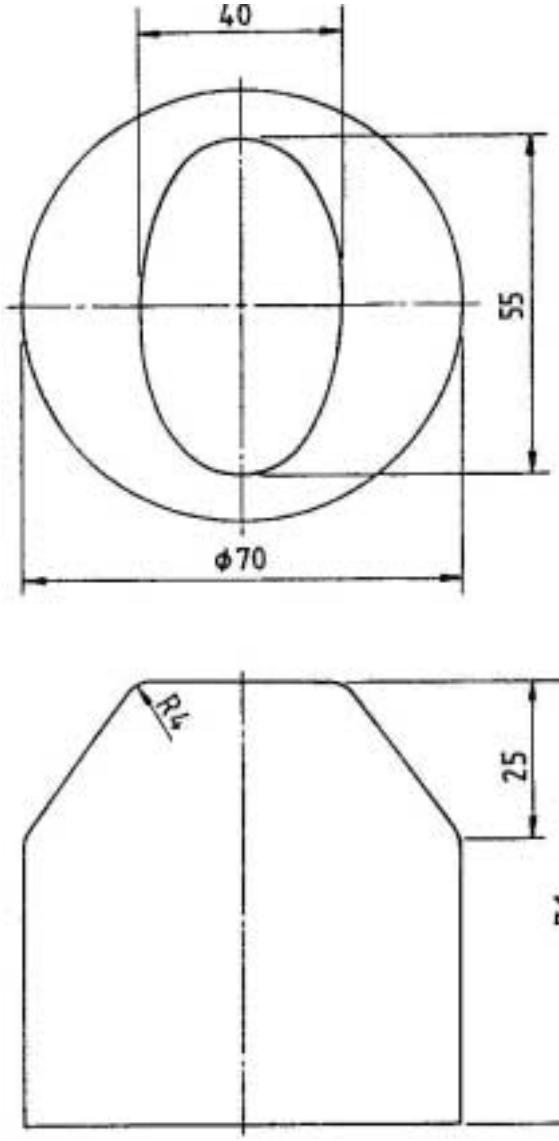

Figure 5. Schematic of Elliptic-circular part [4].

with respect to yield stress (σ_0), punch radius (ra) and thickness (t) respectively. Also the stroke is normalized with respect the instantaneous punch radius (r).

Also results of hemispheric part are given in Figure 4. General shape of an elliptic-circular box is given in Figure 5. The elliptic cross-section of this part is linearly converted to the circle form. Analytic shape of this part can be shown as follows [4]:

$$r = \frac{20 \times 27.5}{\sqrt{(20\mathrm{Cos}\theta)^2 + (27.5\mathrm{Sin}\theta)^2}}(1 - \frac{z}{25}) + 35\frac{z}{25} \quad (18)$$

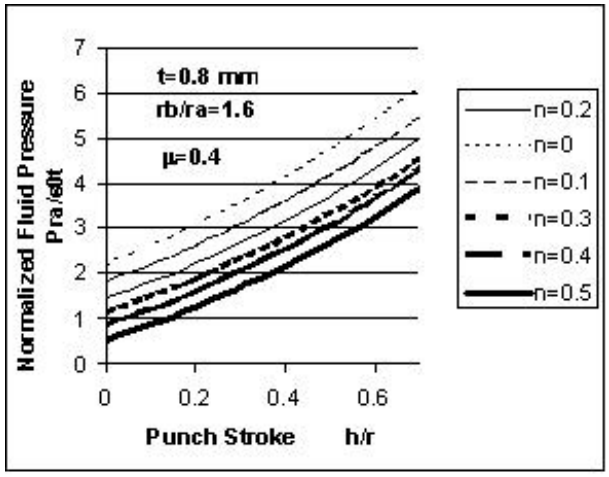

Figure 6. Effect of workhardening Exponent for elliptic-circular part.

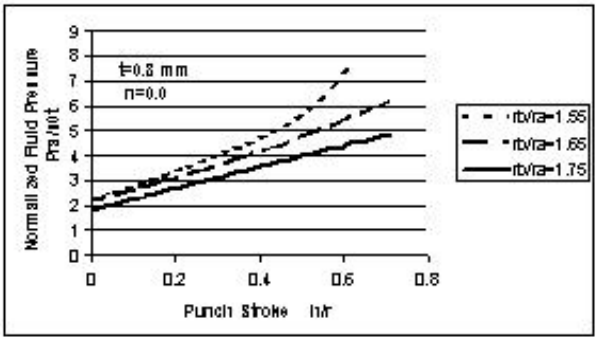

Figure 7. Effect of drawing ratio for elliptic-circular part.

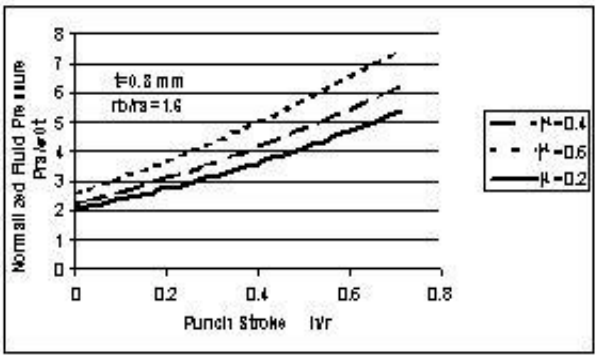

Figure 8. Effect of friction coefficient for elliptic-circular part.

Table 2 shows the information about this part. Figures 6 to 8 show the effects of work hardening, size of blank and friction coefficient on pressure for elliptic-circular box. In these figures r_a denotes the equivalent radius of a circle having the same

TABLE 2. Conditions of Elliptic-Circular Part [4].

Stress-Strain relation(MPa)	Drawing ratio	Initial Blank radius(mm)	Initial Thickness (mm)
$619\times(\bar{\varepsilon}+0.008)^{0.28}$	1.65	57.75	0.8
$619\times(\bar{\varepsilon}+0.008)^{0.28}$	1.75	62.25	0.8
$619\times(\bar{\varepsilon}+0.008)^{0.28}$	1.85	64.75	0.8

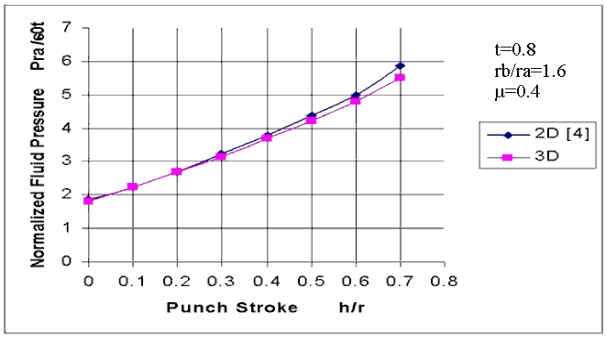

Figure 9. 2D [4] and 3D (present work) calculated results for elliptic-circular part.

cross-sectional area as that of the punch neck. Figure 6 show that the metal with lower work hardening requires more pressure. In other word the metal that has been annealed requires less pressure to be formed. Figure 7 shows the effect of drawing ratio, which is reasonable [6]. Figure 8 reveals the effect of friction coefficient. It can be seen that hydroforming process in high friction is more difficult. In Figure 9 the results of Ref. [4] and present work are compared.

5. DISCUSSIONS

As expected the results obtained by the upper bound is larger than the experimental ones. The trends of pressure variations are very similar in both numerical and experimental results. Figure 9 shows the effect of inclusion of thickness variations on prediction of the hydroforming pressure. Compared with 2D analysis (non varying thickness in reference 4), the present work predicts less forming pressure in the process. This difference becomes more significant when the stroke increases. In fact, in the present work, the material is less constrained just because of inclusion of u_z in the velocity formulations in Equations 11. It must be mentioned that application of more than three terms of Fourier series (Equations 12) does not have significant effect on the results. As a comment we can consider nonlinear terms for $a_i(r)$ and $b_i(r)$. Also we can consider the boundary of velocity discontinuity as a region, such as a triangle region, not only a sharp edge.

6. CONCLUSION

An upper bound based formulation has been developed for prediction of the relation between the pressure and punch stroke in the hydroforming process. Compared with the previous works, the effect of thickness variation has been included in the present formulations. Three parts with different types of geometry have been analyzed and examined with this procedure. The effects of friction and Work hardening have also been considered. Compared with the published experimental results, good agreement was found between the experimental and numerical results. The results also show that consideration of thickness variation causes to predict less forming pressure.

7. NOMENCLATURE

a_i, b_i	optimization parameters relating to the velocity field
A_n, A_p	projected areas of the workpiece and the punch, respectively
$\mathbf{e_r}$, $\mathbf{e_\theta}$, $\mathbf{e_z}$	unit vectors in the cylindrical coordinates

F_p punch force

$F(r, \theta, z)$ punch profile function for a general curved punch shape

h punch stroke

k yield shear stress

$\mathbf{n_p}$, $\mathbf{n}$ unit vectors defined in Figure 1

P fluid pressure

r, θ, z cylindrical coordinates

r_a, r_b equivalent radii of circle having the same cross-section area as that of the punch neck and the initial workpiece, respectively

S_f, S_r surfaces subjected to friction and pressure, respectively

t thickness of workpiece

U* kinematically admissible velocity field

U_n Projection of the velocity vector on the flange zone

U_k inclination component of velocity

u_r, u_θ, u_z radial, circumferential and perpendicular to sheet surface, velocity component, respectively

u_t tangential component of velocity to edge of velocity discontinuity located on plane of flange

U_{nn}, U_{nt} the normal and tangential components of velocity on the flange area, respectively (See Figure 1)

Δu^* velocity discontinuity

V volume of workpiece

V_p punch velocity

V_{pn}, V_{pt} the normal and tangential components of velocity on the punch area, respectively (See Figure 1)

σ_{ij} true stress tensor

σ_{ij}^* stress tensor corresponding to U*

$\dot{\varepsilon}_{ij}^*$ strain tensor corresponding to U*

$\dot{\varepsilon}_r, \dot{\varepsilon}_\theta, \dot{\varepsilon}_z$ Strain rate components in the cylindrical coordinates

μ Coulomb coefficient of friction

ϕ Angle between the punch surface and the flange

ψ, η Angles between velocity components defined in Figure 1

APPENDIX A

Derivation of Equation 5 Referring to Figure 2, we have $\frac{\pi}{2} < \phi < \pi$, so:

$$\cos\phi = -\sqrt{1-\sin^2\phi} = -\sqrt{1-\frac{(\frac{\partial F}{\partial r})^2+(\frac{1}{r}\frac{\partial F}{\partial \theta})^2}{(\frac{\partial F}{\partial r})^2+(\frac{1}{r}\frac{\partial F}{\partial \theta})^2+(\frac{\partial F}{\partial z})^2}} = -\frac{\frac{\partial F}{\partial z}}{\sqrt{(\frac{\partial F}{\partial r})^2+(\frac{1}{r}\frac{\partial F}{\partial \theta})^2+(\frac{\partial F}{\partial z})^2}}, , , \frac{\partial F}{\partial z} > 0 \quad (A.1)$$

$$\tan(\frac{\phi}{2}) = \sqrt{\frac{1-\mathrm{Cos}(\phi)}{1+\mathrm{Cos}(\phi)}} = \frac{\mathrm{Sin}\phi}{1+\mathrm{Cos}\phi} \frac{\sqrt{(\frac{\partial F}{\partial r})^2+(\frac{1}{r}\frac{\partial F}{\partial \theta})^2}}{\sqrt{(\frac{\partial F}{\partial r})^2+(\frac{1}{r}\frac{\partial F}{\partial \theta})^2+(\frac{\partial F}{\partial z})^2}-\frac{\partial F}{\partial z}} \quad (A.2)$$

APPENDIX B

Derivation of Equation 7 Referring to Figure 1:

$$u_{nn}.(\text{volume}) = -V_{pn}.(\text{volume}) \Rightarrow u_{nn} = -V_{pn} \quad (B.1)$$

$$u_{nn} = u_k.\cos(\psi+\eta) \quad (B.2)$$

$$V_{pn} = V_p.\cos(\frac{\phi}{2}) \quad (B.3)$$

Referring to Equations (B.1),(B.2),(B.3):

$$u_k = \frac{-V_p.\cos(\frac{\phi}{2})}{\cos(\psi+\eta)} = \frac{-V_p.\cos(\frac{\phi}{2})}{\cos\psi.\cos\eta-\sin\psi.\sin\eta} \quad (B.4)$$

According to relation $\psi = \frac{\pi}{2} - \frac{\phi}{2}$, finally u_k is given as follows:

$$u_k = \frac{-V_p.\cos(\frac{\phi}{2})}{\sin(\frac{\phi}{2}).\cos\eta - \cos(\frac{\phi}{2}).\sin\eta} = \frac{-V_p}{\tan(\frac{\phi}{2}).\cos\eta - \sin\eta} \quad (B.5)$$

APPENDIX C

Derivation of Equation 9 Equating Equation 7 and Equation 8:

$$\frac{\frac{\partial F}{\partial r}u_r + \frac{1}{r}\frac{\partial F}{\partial \theta}u_\theta + \frac{\partial F}{\partial z}u_z}{\sqrt{(\frac{\partial F}{\partial r})^2 + (\frac{1}{r}\frac{\partial F}{\partial \theta})^2 + (\frac{\partial F}{\partial z})^2}} = \frac{-V_p}{\tan(\frac{\phi}{2})\mathrm{Cos}\eta - \mathrm{Sin}\eta} \quad (C.1)$$

Considering Equations 6, 8 and noting that $\cos\eta = \sqrt{1-\sin^2\eta}$ lead to:

$$\frac{\partial F}{\partial r}u_r + \frac{1}{r}\frac{\partial F}{\partial \theta}u_\theta + \frac{\partial F}{\partial z}u_z = -\frac{\sqrt{(\frac{\partial F}{\partial r})^2 + (\frac{1}{r}\frac{\partial F}{\partial \theta})^2 + (\frac{\partial F}{\partial z})^2}}{\tan(\frac{\phi}{2})}. \left(\sqrt{(u_z - V_p)^2 + u_z^2\tan^2(\frac{\phi}{2})}\right) \quad (C.2)$$

APPENDIX D

Derivation of Equation 11 Considering Equation 10, there exist three variables as u_r, u_θ, u_z. By performing Fourier series it can be written:

$$u_r = \frac{C}{r} + \sum_{i=1}^{\infty}\frac{a_i(r)}{r}\mathrm{Cos}(i\theta) + \sum_{i=1}^{\infty}\frac{b_i(r)}{r}\mathrm{Sin}(i\theta)$$

$$u_\theta = \sum_{i=1}^{\infty}\frac{db_i(r)}{dr}\frac{\mathrm{Sin}(i\theta)}{i} + \sum_{i=1}^{\infty}\frac{da_i(r)}{dr}\frac{\mathrm{Cos}(i\theta)}{i}$$

$$u_Z = -\sum_{i=1}^{\infty} z(\frac{da_i(r)}{rdr} + \frac{db_i(r)}{rdr})\mathrm{Cos}(i\theta) + \sum_{i=1}^{\infty} z(\frac{da_i(r)}{rdr} - \frac{db_i(r)}{rdr})\mathrm{Sin}(i\theta) + a_0(\theta)b_0(r) \quad (D.1)$$

APPENDIX E

Derivation of Equation 15 The velocity discontinuity Δu^* is represented as follows:

$$\Delta u^* = \sqrt{u_t^2 + (u_{nt} + V_{pt})^2} \quad (E.1)$$

According to Figure 1:

$$u_{nt} = u_k.\sin(\psi + \eta) \quad (E.2)$$

$$u_k = \frac{V_p.\cos(\frac{\phi}{2})}{\cos(\psi + \eta)} \quad (E.3)$$

$$V_{pt} = V_p.\sin(\frac{\phi}{2}) \quad (E.4)$$

$$\psi = \frac{\pi}{2} - \frac{\phi}{2} \quad (E.5)$$

Then:

$$u_{nt} = \frac{V_p.\cos(\frac{\phi}{2}).\sin(\psi + \eta)}{\cos(\psi + \eta)} \quad (E.6)$$

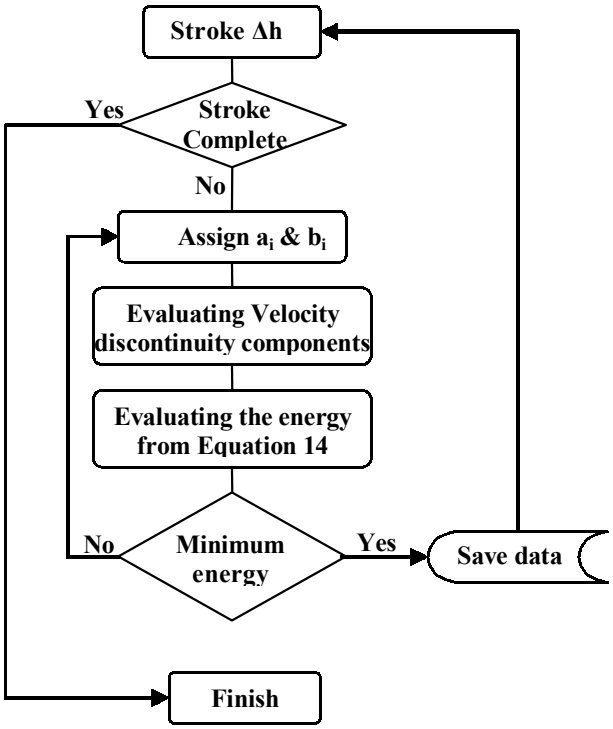

Figure F.1. Logic diagram of solving equations and minimization of total power consumption.

$$\Delta u^* = \sqrt{u_t^2 + u_k^2 . \frac{\cos^2 \eta}{\cos^2(\frac{\phi}{2})}} \qquad (E.7)$$

Noting to relation $u_t^2 + u_k^2 = u_r^2 + u_\theta^2 + u_z^2$, the velocity discontinuity Δu^* is represented as follows:

$$\Delta u^* = \sqrt{u_r^2 + u_\theta^2 + u_z^2 + u_k^2 (\frac{\cos^2 \eta - \cos^2(\frac{\phi}{2})}{\cos^2(\frac{\phi}{2})})} \qquad (E.8)$$

APPENDIX F

Logic diagram of solving equations and minimization of total power consumption is given in Figure F.1.

8. REFERENCES

1. Tirosh, J., Yossifon, S., Eshel, R. and Betzur, A., "Hydroforming Process for Uniform Wall Thickness Products", ***ASME Journal of Engineering for Industry***, Vol. 99, (1977), 685-690.
2. Noh, T. S. and Yang, D. Y., "An Analysis of Hydroforming of Regular Polygonal Boxes", ***Int. J. Mech. Sci.***, Vol. 29, (1987), 139-148.
3. Yang, D. Y. and Noh, T. S., "An Analysis of Hydroforming of Longitudinally Curved Boxes with Regular Polygonal Cross-Section", ***Int. J. Mech. Sci.***, Vol. 32, (1990), 877-890.
4. Yang, D. Y. and Noh, T. S., "A General Formulation for Hydroforming of Arbitrary Shaped Boxes and its Application to Hydroforming of an Elliptic-Circular Box", ***ASME Journal of Manufacturing Science and Engineering***, Vol. 120, (1998), 481-488.
5. John H. Mathews, "Numerical Methods for Computer Science Engineering and Mathematics", Prentice-Hall International, London, (1987).
6. Bagherzadeh, M., "Pressure Estimation in Hydroforming of Sheet Metals", Master of Science Thesis, Sharif University, March (2003).